Photothermal resistivity alignment of optical fibers to SNSPD

M. Baránek,^{1,2} D. Lorenc,^{1,2} T. Ščepka,³ J. Šoltýs,³ I. Vetrova,³ Š. Haščík,³ M. Grajcar,⁴ and P. Neilinger⁴

¹⁾International Laser Centre, Ilkovičova 3, 84104, Bratislava,

Slovakia

²⁾RCQI, Slovak Academy of Sciences, Dúbravská cesta 9, 84511, Bratislava, Slovakia

³⁾Institute of Electrical Engineering, Slovak Academy of Sciences, Dúbravská cesta 9, 84511, Bratislava, Slovakia

⁴⁾Department of Experimental Physics, Comenius University, 84248, Bratislava, Slovakia

(*Electronic mail: martin.baranek@fmph.uniba.sk)

(Dated: 13 November 2025)

We demonstrate a straightforward optoelectronic fiber alignment technique for superconducting nanowire single-photon detectors (SNSPDs) that exploits the temperaturedependent resistance of the nanowire under optical absorption. The target nanowire is
illuminated via the fiber, and the local absorption of light heats the wire, causing a change
in its resistivity. Scanning the fiber over the nanowire, the change in its resistivity is monitored by lock-in amplifier, mapping the spatial photothermal response correlated to absorption and coupling efficiency. The maximum of the response corresponds to optimal fiberSNSPD alignment. This method allows for aligning the fiber to the center of the meander
with sub-micron precision. The response is robust to variations in the angle and height of
the fiber, providing an alternative or complement to fiber-to-chip alignment methods based
on the back-reflection or transmission measurement.

I. INTRODUCTION

Superconducting nanowire single-photon detectors¹ (SNSPDs) combine near-unity detection efficiency,² mHz level dark count rate,³ sub-50 ps timing jitter⁴ and GHz-scale count rate, making them the detector of choice for quantum optics, deep-space communications⁵ and quantum key distribution.^{6,7} The key element of these detectors is the current-biased superconducting nanowire with a width below 100 nm. The absorption of a photon is sufficient to disrupt the superconductivity, resulting in a voltage pulse. The superconductor, from which the nanowires are fabricated, is strongly disordered and, therefore, is characterized by high sheet resistance in the normal state (up to $1 \text{ k}\Omega/\square$),⁸ which usually decreases with increasing temperature. Although intrinsic device performance is governed by material properties, nanowire geometry, and cryogenic biasing conditions, the overall system detection efficiency is constrained by the optical interface required to guide infrared light into micrometer-scale active areas.

To ensure efficient coupling of the light to the nanowire, various alignment methods are utilized,⁹ often relying on wafer etching methods. Notably, in Refs. 2 and 10, a keyhole-shaped window is etched into the substrate by the Bosch process. A zirconium sleeve fits with micrometer precision to the hole, to which the fiber ferrule is inserted. The fiber ferrule is then pushed inside the sleeve up to the point of contact with the SNSPD. This method allows the precise alignment of the fiber and the nanowire with fiber height above the nanowire of less than 10 μ m. However, if the aforementioned mechanical self-alignment is not possible, the back-reflection to the fiber,¹¹ or through-wafer transmission¹² is utilized for SNSPD alignment.

In this work, we present an alternative alignment method grounded in the fundamental principle of SNSPD, specifically the absorption of infrared radiation and the consequent heating of the nanowire. The optical fiber is scanned above the substrate, and by measuring the resistance of the nanowire, the modulated laser beam periodically heats the nanowire (by ≈ 0.1 K), resulting in a small change (in order of $\approx 10^{-5}$) of the resistance. The AC response is then separated by AC coupling and then measured by a lock-in amplifier. The experimental setup is similar to the Lock-in thermography, ¹³ although with the roles of input and output exchanged.

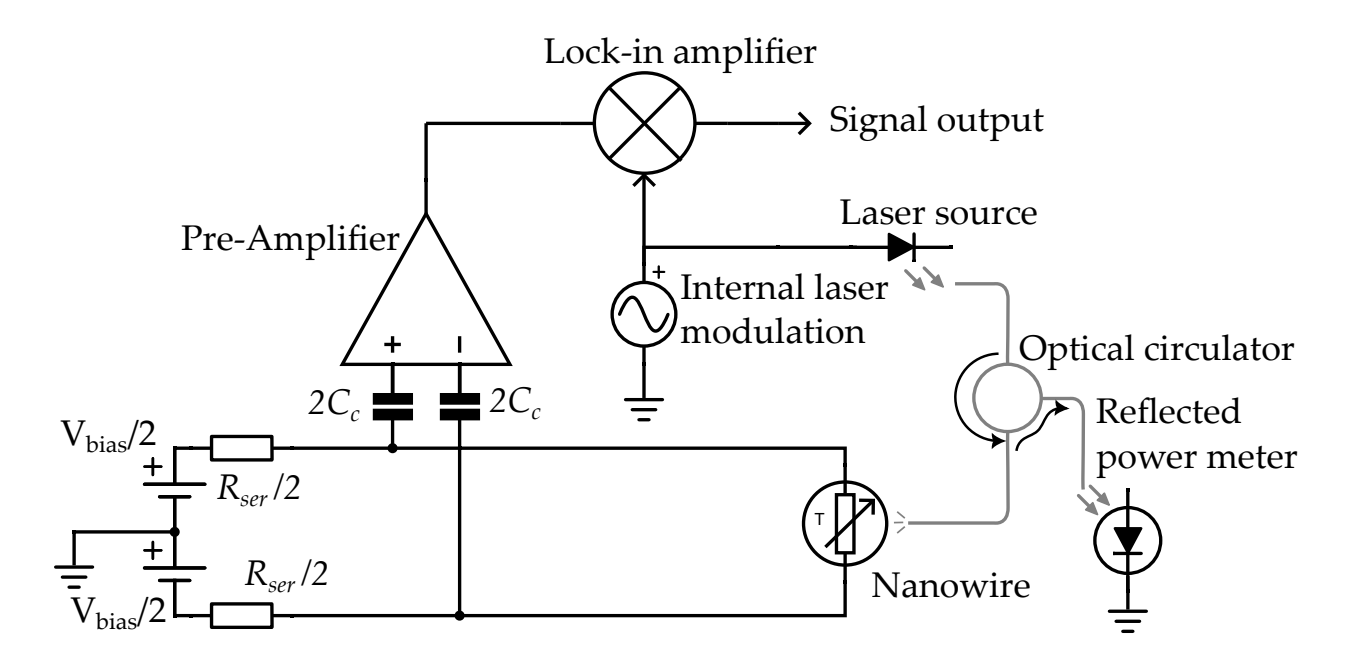


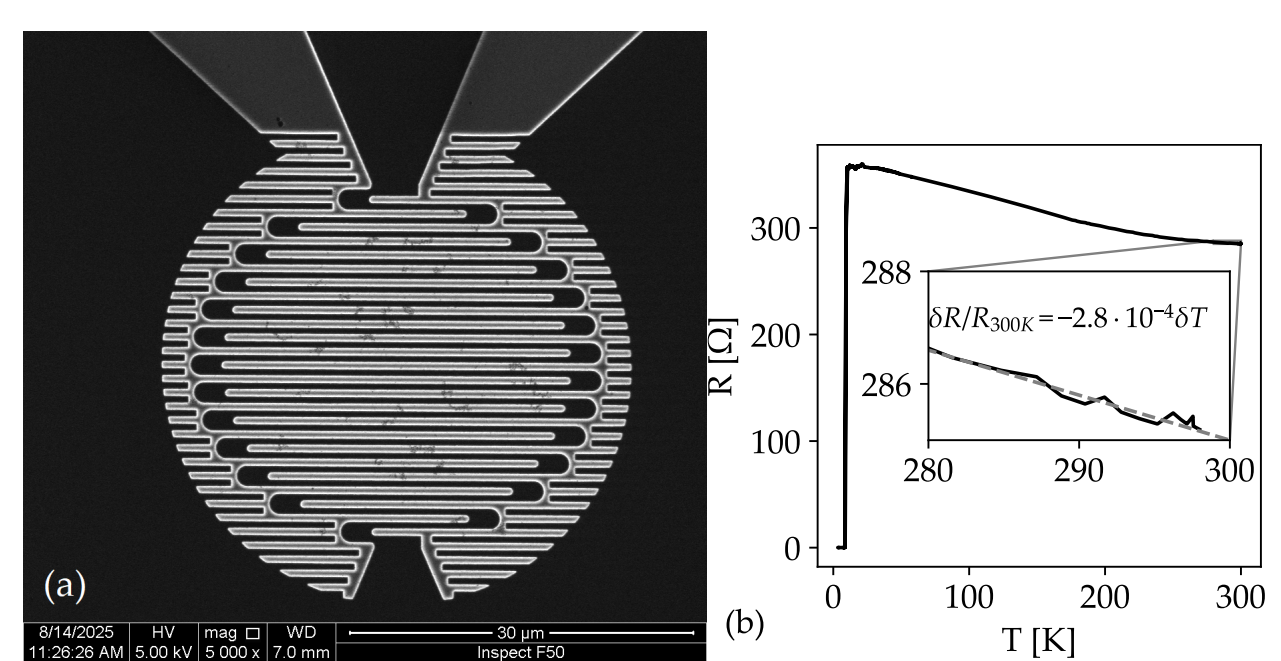
FIG. 1. Scheme of experimental apparatus for photothermal resistivity alignment and optical reflectivity alignment. Optical fibers are grey-colored. The power meter with optical circulator is utilized for back-reflection measurement for comparison to the resistivity measurement.

II. SAMPLE FABRICATION

The NbTiN film was co-sputtered in a reactive magnetron sputtering system in a mixed atmosphere of N_2 and Ar. Film was deposited on commercial c-cut sapphire substrates at room temperature. Two separate source targets with niobium and titanium were installed in the ultrahigh vacuum chamber operating at a base pressure of 1×10^{-7} Torr. The working pressure was kept at 3 mTorr, while Ar and N_2 gas flows were 50 and 5 sccm, respectively. The Nb and Ti targets were controlled with a 80 W DC and 240 W RF power sources, respectively. The deposition rates were initially calibrated on thicker films.

The fabrication process involved patterning a meander-shaped nanowire via electron beam lithography in PMMA resist and then transferring the pattern using reactive ion etching (RIE) with CF₄ plasma. We fabricated a 7.5 nm thick NbTiN test sample, with sheet resistance $R_s = 285 \Omega$. The resulting structure features a 30 μ m inner diameter, a 500 nm nanowire width w, 500 nm spacing s, corresponding to fill factor f = w/(w+s) of 0.5.

The ground plane and meander were wire-bonded with aluminium wire. The transport properties were characterized down to 4 K. The residual resistivity ratio is 0.8 and the critical temperature



is 9 K. The test nanowire, shown in Fig. 2a was fabricated with diameter of 30 μ m and width of

FIG. 2. (a) SEM image of the NbTiN nanowire. (b) Transport measurement of the NbTiN film. The inset shows the detail of the resistivity dependence in the vicinity of room temperature, where the alignment was carried out. The extracted temperature coefficient ratio at room temperature is $\alpha = -2.8 \times 10^{-4}$.

500 nm resulting in a comparable resistance to the common dimensions of \approx 10 μ m and 100 nm.² The signal strength is proportional to the change of resistance:

$$V_{response} \propto \delta R(T) = R(300\text{K}) \times \alpha \times (T - 300\text{K}),$$
 (1)

where α is the temperature coefficient of resistance, given by the residual resistivity ratio.

III. OPTICAL ABSORPTION

The optical absorption A of a metallic film in the limit of thin films (thickness $d < \lambda$) with wavelength-dependent sheet resistance $R_s(\lambda)$ on a substrate with refractive index n_{sub} is given as follows¹⁴:

$$A(\lambda) = \frac{4R_s/Z_0}{((R_s(\lambda)/Z_0)(n_{sub}+1)+1)^2},$$
(2)

where $Z_0 = 377\Omega$ is the vacuum impedance. A common approximation is to neglect the wavelength dependence of R_s and simply utilize its DC value estimated by four-probe transport measurement. For example, for our film, $R_s = 285\Omega$ would lead to absorption of A = 31.9%.

However, for strongly disordered films, quantum corrections to the conductivity are present and the DC conductivity $\sigma_{DC} = 1/(R_s d)$ is strongly suppressed compared to the optical conductivity at 1550 nm. ^{15,16} The optical conductivity of the film $\sigma = \sigma_r + j\sigma_i$ is determined by spectroscopic ellipsometry, shown in Fig. 3. The DC conductivity is suppressed by 30% compared to its value at 1550 nm. The corresponding absorption A, reflection R, and transmission spectra T of the thin film, calculated from Fresnel equations, are shown in Fig. 3. Its value at $\lambda = 1550$ nm is A = 34.4%.

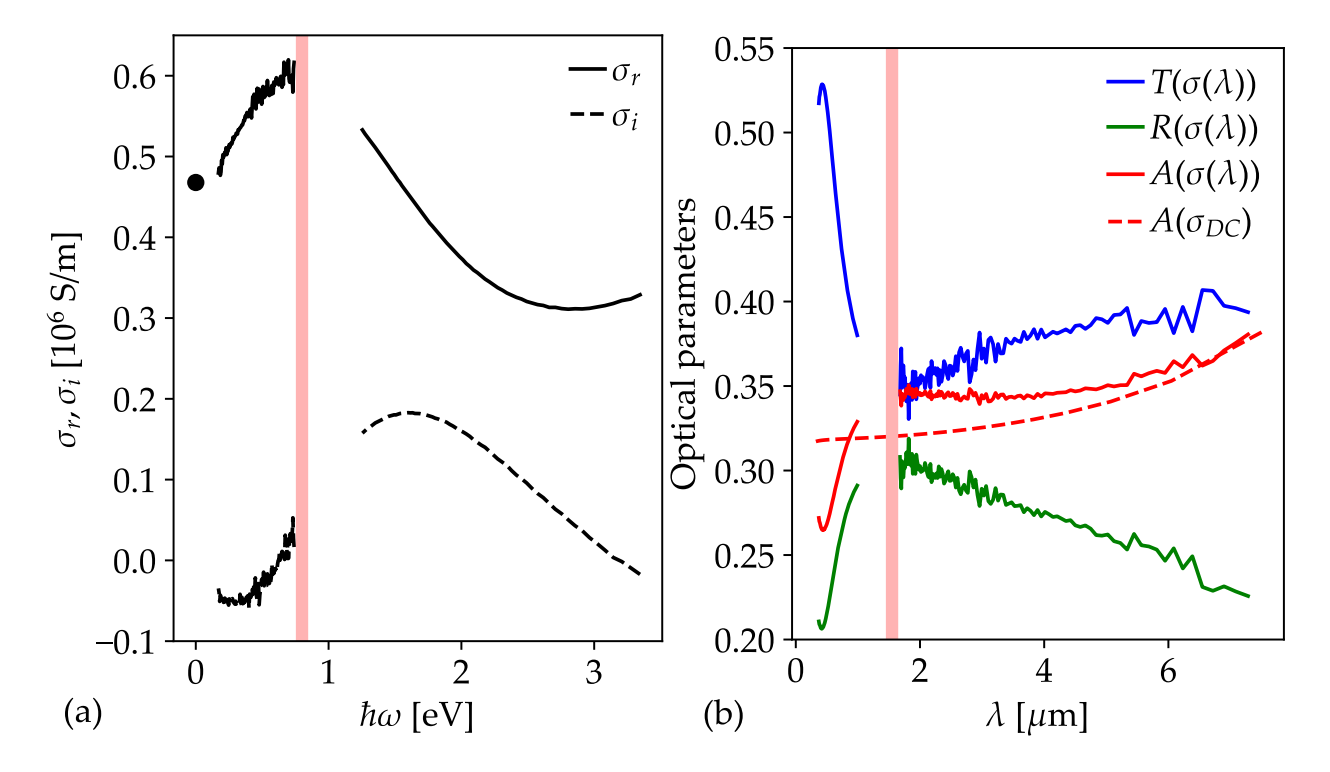


FIG. 3. (a) Optical conductivity determined from spectroscopic ellipsometry and DC conductivity from four-point measurement (circle). (b) transmission, reflectivity, and absorbance spectra calculated from conductivity using Fresnel equations at 0° angle of incidence. Red vertical line is guideline for $\lambda=1550$ nm. Red dashed line represents absorption assuming DC sheet resistance of the sample.

Given that the nanowire width and spacing are significantly smaller than the irradiation wavelength, the effective medium approximation can be used.¹⁷ Therefore, a sufficiently narrow meandering nanowire of film sheet resistance R_s with a fill factor f can be approximated as a thin film with sheet resistance $R_s^{eff} = R_s/f$. The feasibility of the effective medium approximation for common SNSPD designs was also verified numerically in Ref. 18.

The resulting absorption of the fabricated nanowire is $A^{NW} = 26.3\%$ for the conductivity at

1550 nm. In the case of 500 nm wide separation between nanowires, the absorption may decrease due to the light leakage. Moreover, polarization dependence is stronger for sub-100 nm nanowires.

The temperature distribution in thin films can be determined either through analytical methods (see, for instance, Ref. 19) or through numerical simulations, which allow for the entire meander to be modeled. The frequency and displacement dependence of the photothermal response is governed by thermal properties of substrate, thin film, and their interfacial thermal resistance (Kapitza resistance, see, e.g. Ref. 20).

IV. APPARATUS

The wirebonded nanowire was placed on a PCB, which was attached to the motorized XYZ nano-positioning stage (Attocube ECSxy5050, ECSz5050), as shown in Fig. 4. First, the fiber was positioned at starting position utilizing manual micro-positioners. Then, the scan was performed with nano-positioners with 50 nm repeatability.

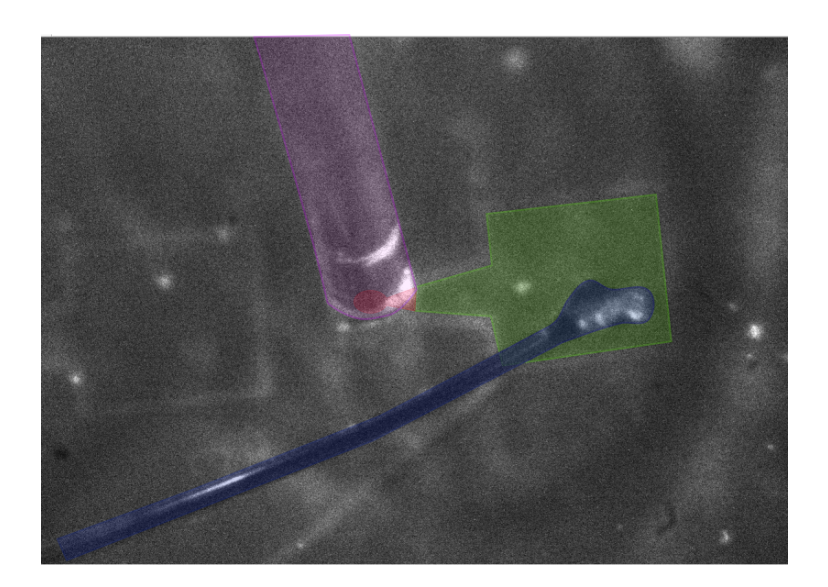


FIG. 4. Pseudocolored photo of fiber (purple) suspended over meander (red). Bonding pad of the meander (green) is aluminum wire-bonded (blue). Grounding wire-bonds are not visible in the photo.

The illuminating laser source (HP 8168E, λ =1550 nm) was AC modulated and the photothermal response was measured by SRS SR830 Lock-in amplifier locked to the laser modulation frequency f_{mod} with the AC-coupled FEMTO DLPVA-100-B-D preamplifier. To prevent damage to the lock-in/preamplifier, additional DC blocks were utilized.

The DC bias was realized as a balanced differential voltage through a pair of 12V A27 batteries, to eliminate ground loops, noise from the current source, and interference caused by high voltage pulses from piezo actuators in the nano-positioner. The small size of the batteries allowed them to be placed in close proximity to the nanowire. The ground was then connected to the apparatus grounding point. All wires were twisted pairs with grounded shielding. The sample on a PCB was placed on top of the grounded baseplate.

To maximize the output signal at given bias voltage V_{bias} , the serial resistance R_{ser} should be impedance-matched to the nanowire resistance R_{nw} (e.g. 400 k Ω). This biasing circuit provided 30 μ A of bias current/12 V of bias voltage to the nanowire, resulting in 30 μ V response. The equivalent scheme for the readout circuit is presented in Fig. 5, where C_w is the cable capacitance, C_c is the AC coupling capacitance, and R_{amp} and C_{amp} are input resistance and capacitance of the first amplification stage. The AC voltage generated at nanowire is given as $V_{AC} = \delta R \times V_{bias}/(R_{nw} + R_{ser})$, where δR is given by eq. 1.

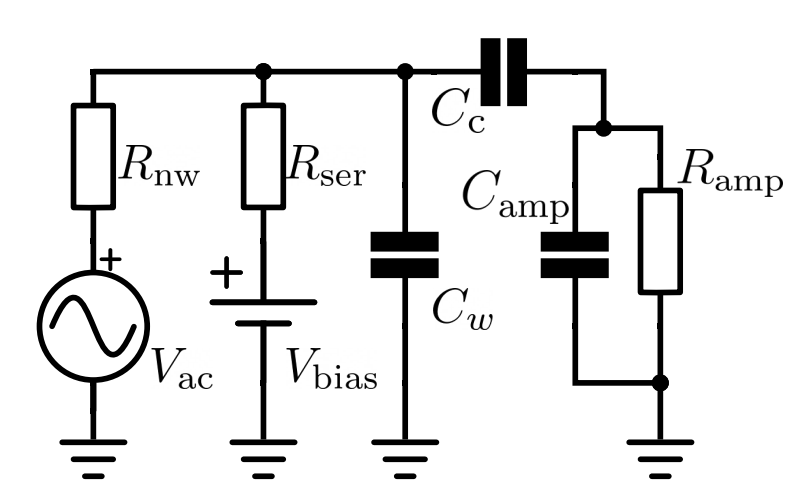


FIG. 5. Equivalent scheme for the readout circuit.

V. RESULTS

The XY-scan of the photothermal response at lowest height with 1.5 μ m step is shown in Fig. 6. The maximum response amplitude, corresponding to the perfect alignment of the fiber and the meander-shaped nanowire, is 23 μV_{RMS} . When the fiber is far from the center of the nanowire, the temperature and thus the resistance of the nanowire are not modulated, and the signal amplitude drops below 1 μ V, corresponding to SNR of approximately 20. Due to the high

output impedance and the low signal amplitude, the resulting signal current is ≤ 100 pA, thus, the choice of modulation frequency is limited by the capacitance of the wires (C_w) . This can be seen in Fig. 7, where a high frequency cutoff is clearly visible at frequencies of ≈ 1 kHz. Therefore, the XY scan was performed at $f_{mod} = 871$ Hz.

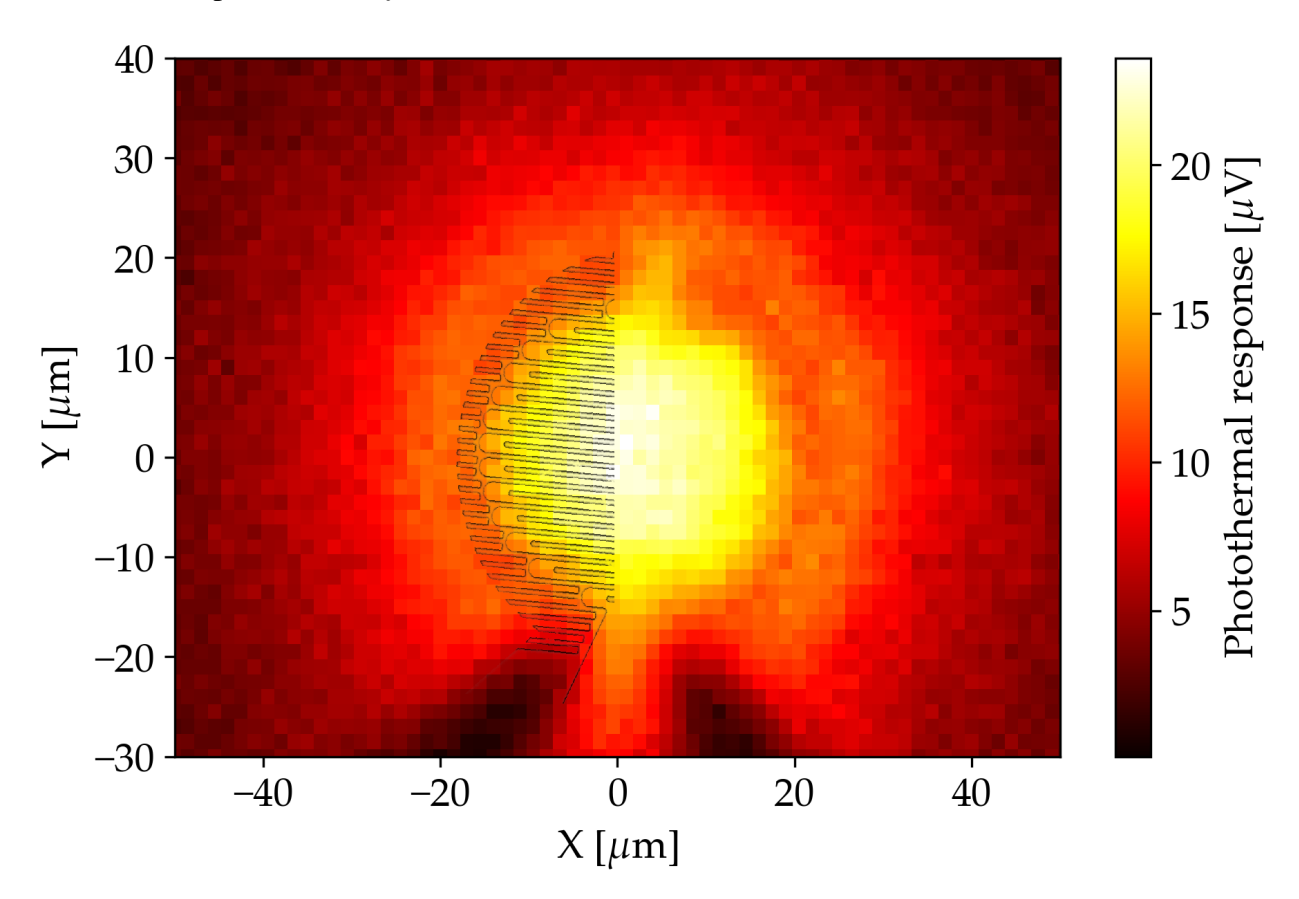


FIG. 6. XY scan of photothermal response at lowest height, with 1.5 μ m step. To visualize the detection sensitivity, we superimposed SEM image of the test nanowire from Fig. 2a with enhanced contrast.

The cross-sections measured with 500 nm steps in Fig.8 show that the resolution is limited by the beam width and by the noise of the measurement, rather than by the precision of the nanopositioning.

To compare the performance of the photothermal response, we performed back-reflection optical measurement, utilizing an optical in-fiber circulator and Thorlabs S154C photodiode in PM100D power meter, shown in Fig. 1. The scans are shown in Fig. 9. The polarization dependence of a 500 nm wide nanowire ($w \approx \lambda/3$) differs significantly from the sub-100 nm ($w \approx \lambda/15$) state-of-the-art SNSPDs.

The comparison of the height sweep scans (presented in Fig. 10) reveals a significantly stronger

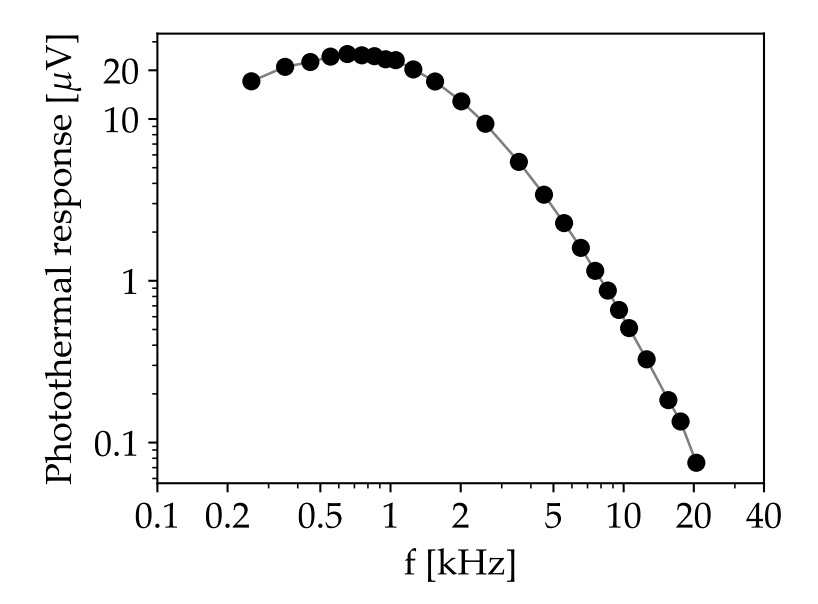


FIG. 7. Dependence of photothermal response on laser modulation frequency f_{mod} . Low frequency response is limited by the AC coupling of the circuit, while high frequency response is limited by high impedance and cable capacitance.

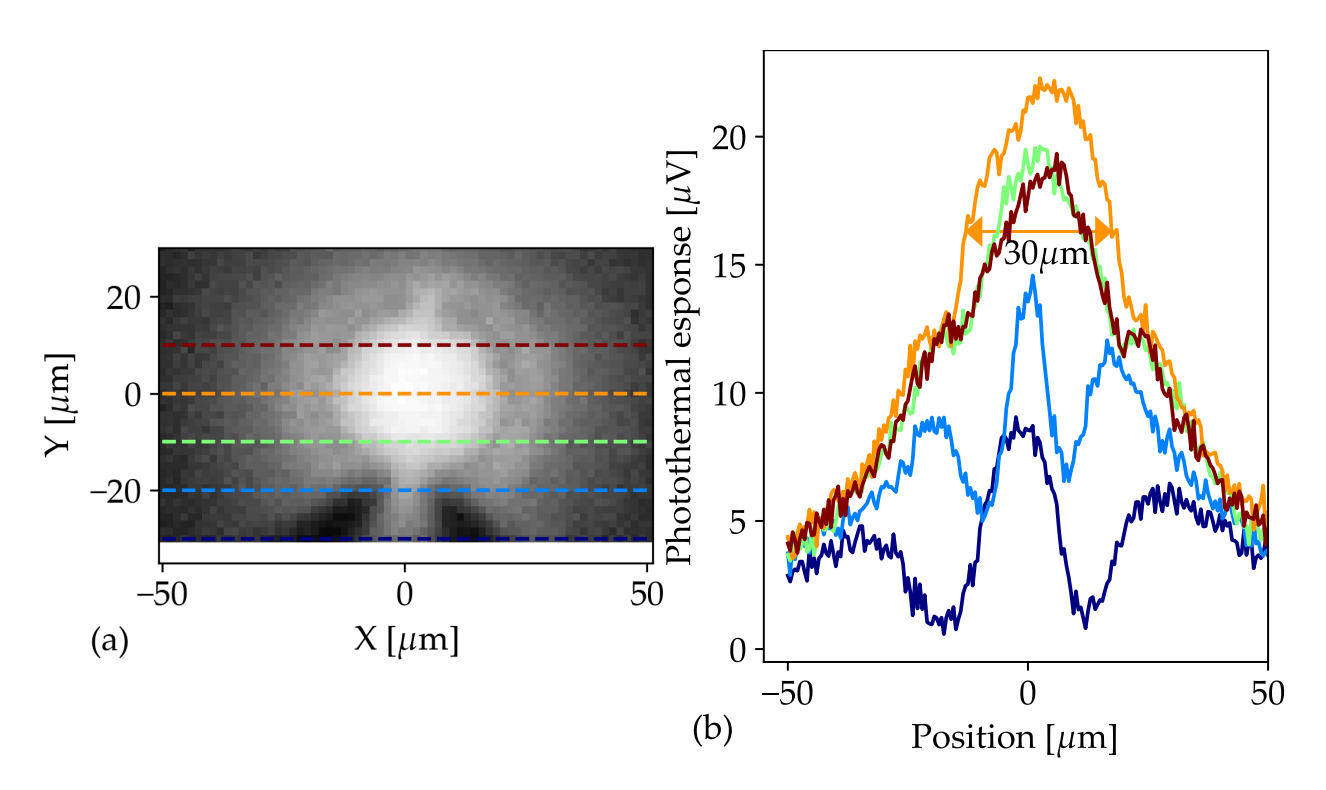


FIG. 8. (a) XY scan of photothermal response. Horizontal lines show the cross-sections. (b) Cross-sections measured with 500 nm steps.

height dependence in the back-reflection measurement, as it requires coupling of the diverging

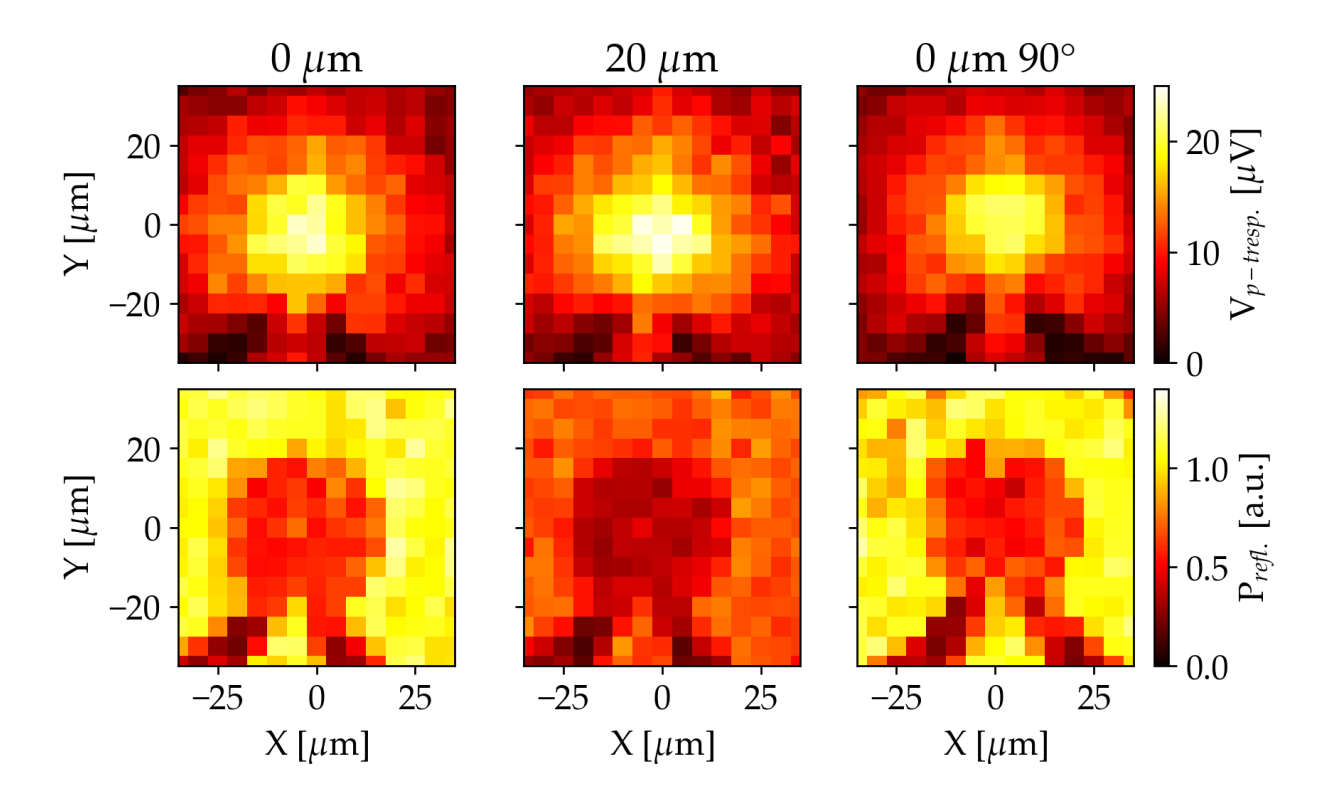


FIG. 9. Photothermal response of the SNSPD (top row) and back-reflection measurement (bottom row) at different heights (left and center) and for sample rotated by 90° (right) to test the polarization sensitivity.

light back into the 10 μ m fiber core.

VI. CONCLUSION

We have proposed and demonstrated the feasibility of a simple photothermal alignment technique for SNSPDs that exploits the temperature dependence of the nanowire resistance to generate a signal detectable by a lock-in upon local heating by a modulated optical beam irradiating the active area. Using a laser with modulation intensity of $\approx 400 \ \mu\text{W}$, we obtained a peak response of 23 μV_{RMS} with signal-to-noise ratio SNR \approx 20 and spatial resolution in the range of $\approx \mu\text{m}$, with fine height scans resolved to 250 nm and XY scans to 500 nm.

The presented method requires 3D alignment means similar to optical methods, such as back-reflection measurement, with the advantage of lower sensitivity to the fiber height and incident angle misalignment. Thus, this photothermal alignment is an accessible method that is fabrication-compatible with the SNSPD production and can substitute existing fiber-to-chip alignment methods or complement them to improve reproducibility and throughput in SNSPD finalization. More-

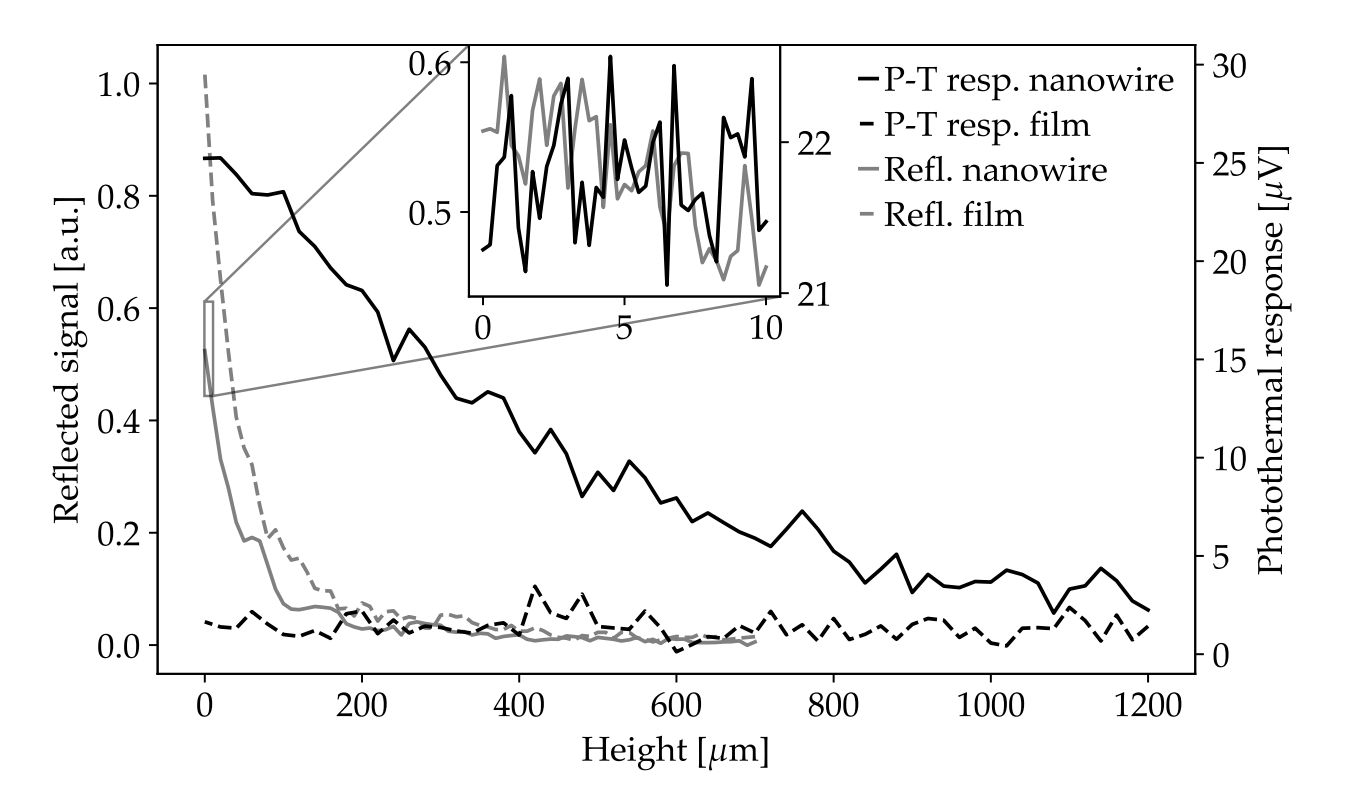


FIG. 10. Comparison of the height scans of the photothermal and back-reflected method. The inset shows the detail of the height scans in the vicinity of the surface ($<10 \mu m$) with 250 nm steps.

over, the presented method can be used for in-situ coupling efficiency evaluation of the SNSPD detector during cooldown and could be utilized in other fields of physics, such as, for example, in the study of heat transfer in nanostructures, ^{21,22} in thin films in general, ^{23,24} or as an additional independent measurement channel for time-domain thermoreflectance measurements ^{25,26} for sufficiently conductive samples. Although beyond the scope of this paper, we are currently investigating the feasibility of using this method to extract the heat capacity and thermal conductivity of the thin films.

FUNDING

This work was supported by the project skQCI (101091548), funded by the European Union (DIGITAL) and the Recovery and Resilience Plan of the Slovak Republic.

CONFLICT OF INTERESTS

The authors have no relevant financial or non-financial interests to disclose.

AUTHOR CONTRIBUTIONS

Conceptualization - PN (lead), MB (supporting); Data Curation - MB (lead); Formal Analysis - MB (lead), PN (supporting); Funding Acquisition - MG (lead), PN (supporting); Methodology - MB (equal), PN (equal), MG (supporting); Project Administration - MG (lead), PN (supporting); Resources - MB (equal), PN (equal), DL (equal), TŠ (equal), JŠ (equal), IV (equal), ŠH (equal), MG (supporting); Software - MB (equal), DL (equal); Supervision - PN (lead); Validation - MB (lead), DL (supporting), PN (supporting); Visualization - MB (lead); Writing/Original Draft Preparation - MB (equal), PN (equal), JŠ (supporting), TŠ (supporting); Review and Editing - all authors (equal).

DATA AVAILABILITY STATEMENT

The data that support the findings of this study are available from the corresponding author upon reasonable request.

REFERENCES

- ¹G. N. Goltsman, O. Okunev, G. Chulkova, A. Lipatov, A. Semenov, K. Smirnov, B. Voronov, A. Dzardanov, C. Williams, and R. Sobolewski, Applied Physics Letters **79**, 705 (2001), https://pubs.aip.org/aip/apl/article-pdf/79/6/705/18559493/705_1_online.pdf.
- ²J. Chang, J. W. N. Los, J. O. Tenorio-Pearl, N. Noordzij, R. Gourgues, A. Guardiani, J. R. Zichi, S. F. Pereira, H. P. Urbach, V. Zwiller, S. N. Dorenbos, and I. Esmaeil Zadeh, APL Photonics **6**, 036114 (2021), https://pubs.aip.org/aip/app/article-pdf/doi/10.1063/5.0039772/14572142/036114_1_online.pdf.
- ³A. S. Mueller, B. Korzh, M. Runyan, E. E. Wollman, A. D. Beyer, J. P. Allmaras, A. E. Velasco, I. Craiciu, B. Bumble, R. M. Briggs, L. Narvaez, C. P. na, M. Spiropulu, and M. D. Shaw, Optica **8**, 1586 (2021).
- ⁴F. Najafi, A. Dane, F. Bellei, Q. Zhao, K. A. Sunter, A. N. McCaughan, and K. K. Berggren, IEEE Journal of Selected Topics in Quantum Electronics **21**, 1 (2015).
- ⁵E. E. Wollman, J. P. Allmaras, A. D. Beyer, B. Korzh, M. C. Runyan, L. Narváez, W. H. Farr, F. Marsili, R. M. Briggs, G. J. Miles, and M. D. Shaw, Opt. Express **32**, 48185 (2024).

- ⁶Y.-A. Chen, Q. Zhang, T.-Y. Chen, W.-Q. Cai, S.-K. Liao, J. Zhang, K. Chen, J. Yin, J.-G. Ren, Z. Chen, S.-L. Han, Q. Yu, K. Liang, F. Zhou, X. Yuan, M.-S. Zhao, T.-Y. Wang, X. Jiang, L. Zhang, W.-Y. Liu, Y. Li, Q. Shen, Y. Cao, C.-Y. Lu, R. Shu, J.-Y. Wang, L. Li, N.-L. Liu, F. Xu, X.-B. Wang, C.-Z. Peng, and J.-W. Pan, Nature **589**, 214 (2021).
- ⁷D. Ribezzo, M. Zahidy, I. Vagniluca, N. Biagi, S. Francesconi, T. Occhipinti, L. K. Oxenløwe, M. Lončarić, I. Cvitić, M. Stipčević, v. Pušavec, R. Kaltenbaek, A. Ramšak, F. Cesa, G. Giorgetti, F. Scazza, A. Bassi, P. De Natale, F. S. Cataliotti, M. Inguscio, D. Bacco, and A. Zavatta, Advanced Quantum Technologies 6, 2200061 (2023), https://onlinelibrary.wiley.com/doi/pdf/10.1002/qute.202200061.
- ⁸P. Zolotov, S. Svyatodukh, A. Divochiy, V. Seleznev, and G. Goltsman, Applied Physics Letters **122**, 152602 (2023).
- ⁹E. Dauler, M. Grein, A. Kerman, F. Marsili, S. Miki, S. Nam, M. Shaw, H. Terai, V. Verma, and T. Yamashita, Optical Engineering **53** (2014), 10.1117/1.OE.53.8.081907.
- ¹⁰A. J. Miller, A. E. Lita, B. Calkins, I. Vayshenker, S. M. Gruber, and S. W. Nam, Opt. Express 19, 9102 (2011).
- ¹¹K. Erotokritou, R. M. Heath, G. G. Taylor, C. Tian, A. Banerjee, A. Casaburi, C. M. Natarajan, S. Miki, H. Terai, and R. H. Hadfield, Superconductor Science and Technology 31, 125012 (2018).
- ¹²J.-L. F.-X. Orgiazzi and A. H. Majedi, IEEE Transactions on Applied Superconductivity **19**, 341 (2009).
- ¹³O. Breitenstein and M. Langenkamp, *Lock-in Thermography-Basics and Use for Functional Diagnostics of Electronic Components* (Springer Dordrecht, 2003).
- ¹⁴A. Semenov, B. Günther, U. Böttger, H.-W. Hübers, H. Bartolf, A. Engel, A. Schilling, K. Ilin, M. Siegel, R. Schneider, D. Gerthsen, and N. A. Gippius, Phys. Rev. B 80, 054510 (2009).
- ¹⁵P. Neilinger, J. Greguš, D. Manca, B. Grančič, M. Kopčík, P. Szabó, P. Samuely, R. Hlubina, and M. Grajcar, Phys. Rev. B 100, 241106 (2019).
- ¹⁶S. Kern, P. Neilinger, M. Poláčková, M. Baránek, T. Plecenik, T. Roch, and M. Grajcar, Phys. Rev. B 110, 245131 (2024).
- ¹⁷S. Moon and D. Kim, J. Opt. Soc. Am. A **23**, 199 (2006).
- ¹⁸M. Baránek, P. Neilinger, S. Kern, and M. Grajcar, Optical and Quantum Electronics **56**, 1730 (2024).

- ¹⁹J. A. António Tadeu and N. Simões, Computer Modeling in Engineering & Sciences **6**, 43 (2004).
- ²⁰T. Nguyen, A. Tavakoli, S. Triqueneaux, R. Swami, A. Ruhtinas, J. Gradel, P. Garcia-Campos, K. Hasselbach, A. Frydman, B. Piot, M. Gibert, E. Collin, and O. Bourgeois, Journal of Low Temperature Physics 197, 348 (2019).
- ²¹M. Sidorova, A. D. Semenov, A. Zaccone, I. Charaev, M. Gonzalez, A. Schilling, S. Gyger, and S. Steinhauer, Phys. Rev. B **110**, 134513 (2024).
- ²²C. Romeo, A. Baldi, and S. H. C. Askes, APL Materials **13**, 080601 (2025).
- ²³C. Grosse-Kockert, M. A. Ras, D. May, A. Cremieux-Trives, F. Löffler, and B. Wunderle, 2022 28th International Workshop on Thermal Investigations of ICs and Systems (THERMINIC), 1 (2022).
- ²⁴C. Dames, Annual Review of Heat Transfer **16**, 7 (2013).
- ²⁵C. Yuan, R. Hanus, and S. Graham, Journal of Applied Physics **132**, 220701 (2022).
- ²⁶R. Mohan, S. Khan, R. B. Wilson, and P. E. Hopkins, Nature Reviews Methods Primers **5**, 55 (2025).